Catalysis Today 265 (2016) 103–110

Contents lists available at ScienceDirect

Catalysis Today

journal homepage: www.elsevier.com/locate/cattod

Hydrogen production by steam reforming of ethanol over dual-templated Ni–Al_2O_3 catalyst

Seung Ju Han, Yongju Bang, Ji Hwan Song, Jaekyeong Yoo, Seungwon Park, Ki Hyuk Kang, In Kyu Song*

School of Chemical and Biological Engineering, Institute of Chemical Processes, Seoul National University, Shinlim-dong, Kwanak-ku, Seoul 151-744, South Korea

ARTICLE INFO

Article history:
Received 10 June 2015
Received in revised form 22 July 2015
Accepted 26 July 2015
Available online 7 August 2015

Keywords:
Hydrogen production
Steam reforming of ethanol
Mesoporous Ni–Al_2O_3 catalyst
Nickel surface area
Ethanol adsorption capacity

ABSTRACT

A dual-templated Ni–Al_2O_3 catalyst (SINA) was prepared by a single-step evaporation-induced self-assembly (EISA) method using P123 and ionic liquid as templates. For comparison, a P123-templated Ni–Al_2O_3 catalyst (SNA) was also prepared by a single-step evaporation-induced self-assembly (EISA) method in the absence of ionic liquid. Both catalysts were applied to the hydrogen production by steam reforming of ethanol. The effect of ionic liquid addition on the physicochemical properties and catalytic activities of the catalysts was investigated. Although both catalysts exhibited a mesoporous structure, SINA catalyst retained higher surface area and larger pore volume than SNA catalyst. It was also revealed that SINA catalyst retained higher nickel surface area and higher ethanol adsorption capacity than SNA catalyst. In the hydrogen production by steam reforming of ethanol, both catalysts exhibited a stable catalytic performance with complete conversion of ethanol. However, SINA catalyst exhibited higher hydrogen yield than SNA catalyst. High surface area and high nickel dispersion of SINA catalyst were responsible for its high hydrogen yield. The addition of ionic liquid as a co-template in the preparation of mesoporous SINA catalyst increased surface area, nickel dispersion, and catalytic activity of the catalyst.

1. Introduction

With increasing concerns about dependence on fossil fuel and environmental problems, the need for alternative energy sources has been emphasized [1,2]. Hydrogen has been considered as one of the promising candidates for alternative energy carrier because of its non-toxicity, abundance, and high specific energy density (ca. 120.7 kJ/g) [3]. Many hydrocarbons such as gasoline, natural gas, methanol, propane, and ethanol can serve as a hydrogen source. However, most hydrogen energy is currently produced from non-renewable natural gas through the reforming processes, which is still based on fossil fuel system [4]. Although natural gas is the most common source for hydrogen production, ethanol, which is biodegradable, renewable, and non-toxic, can serve as an attractive hydrogen source [5].

For hydrogen production by steam reforming of ethanol, Ni-based catalyst such as Ni/Al_2O_3 has been widely used because of its high C—C bond cleavage activity and low cost [6,7]. However, it is known that Ni/Al_2O_3 catalyst experiences severe deactivation in the steam reforming of ethanol because acid sites of Al_2O_3 promote dehydration reaction of ethanol, forming ethylene which acts as a coke precursor [8]. In order to develop a Ni/Al_2O_3 catalyst with high catalytic activity and long term stability, there have been many attempts to modify physicochemical properties of Ni/Al_2O_3 catalyst. For example, alkaline oxides such as MgO and CaO have been added to Ni/Al_2O_3 catalyst in order to promote reactivity toward water and to retard dehydration reaction by neutralizing acid sites of Al_2O_3 [9]. It is also attempted that the addition of Ce and La to Ni/Al_2O_3 catalyst prevents the formation of carbon filaments which are responsible for catalyst deactivation [7]. Ni–Al_2O_3–ZrO_2 xerogel catalyst has also been investigated because ZrO_2 can increase the stability of the catalyst in the steam reforming of ethanol [10–12].

In order to improve physicochemical properties of materials, there have been many researches on templating methods. In particular, soft templates such as surfactants have been widely used for the synthesis of ordered mesoporous materials [13–15]. Since the discovery of supramolecular-templated mesoporous materials such as MCM-41 and M41S, ordered mesoporous alumina has been successfully prepared by an evaporation-induced self-assembly (EISA) method using P123 as a surfactant material [16–18]. Mixtures of templates have also been employed to achieve mesoporous

* Corresponding author.
E-mail address: inksong@snu.ac.kr (I.K. Song).

http://dx.doi.org/10.1016/j.cattod.2015.07.041
0920-5861/

structure and hierarchically porous structure. It is known that the surfactant mixtures can form three compound models; individual micelle, compound micelle, and micelle of the surfactant and single surfactant of the other [19–21]. Recently, ionic liquids have been used as templates to prepare microporous and mesoporous materials by taking advantage of their amphiphilic property [22]. Long chain ionic liquids, which are composed of ionic head and organic chain, have induced self-aggregation, demonstrating their potential usage as templates [23–26]. For example, C_{16}mimCl has been used as a template to prepare monolithic supermicroporous silica with lamellar order via nanocasting technique [27,28].

In this work, a dual-templated Ni–Al_2O_3 catalyst was prepared by a single-step evaporation-induced self-assembly (EISA) method using P123 and ionic liquid (1-hexadecyl-3-methylimidazolium chloride) as templates. For comparison, a P123-templated Ni–Al_2O_3 catalyst was also prepared by a similar method in the absence of ionic liquid. The effect of ionic liquid addition on the physicochemical properties and catalytic activities of the catalysts was investigated.

2. Experimental

2.1. Preparation of dual-templated Ni–Al_2O_3 catalyst

A dual-templated Ni–Al_2O_3 catalyst (denoted as SINA) was prepared by a single-step evaporation-induced self-assembly (EISA) method using P123 and ionic liquid as templates according to the similar methods reported in the literature [16]. 2.3 g of $(EO)_{20}(PO)_{70}(EO)_{20}$ triblock copolymer (Pluronic P123, Sigma–Aldrich) and 0.5 g of ionic liquid (1-hexadecyl-3-methylimidazolium chloride monohydrate, Acros) were dissolved in anhydrous ethanol (50 ml) at room temperature with constant stirring for 4 h (Solution A). 4.3 g of aluminum precursor (aluminum isopropoxide, Sigma–Aldrich) and 0.94 g of nickel precursor (nickel nitrate hexahydrate, Sigma–Aldrich) were then added into the solution A (Solution B). 4.7 ml of nitric acid (69%) was added to the solution B for complete homogenization and hydrolysis of metal precursors (Solution C). The solution C was stirred for 5 h, and subsequently, self-assembly of micelle structure was induced through solvent evaporation at 60 °C for 48 h without stirring. The resulting solid was calcined at 550 °C for 5 h at a heating rate of 1 °C/min to yield SINA catalyst.

For comparison, a P123-templated Ni–Al_2O_3 catalyst (denoted as SNA) was prepared by a single-step evaporation-induced self-assembly (EISA) method in the absence of ionic liquid (C_{16}mimCl). 2.3 g of P123 was used as a template for the preparation of P123-templated Ni–Al_2O_3 catalyst. The remaining preparation procedures for SNA catalyst were identical to those for SINA catalyst. After EISA process, the resulting solid was calcined at 550 °C for 5 h at a heating rate of 1 °C/min to yield SNA catalyst. Ni content in the SNA and SINA catalysts was fixed at 15 wt%.

2.2. Characterization

Textural properties of SNA and SINA catalysts were determined by N_2 adsorption–desorption experiments using a BELSORP-mini II (BEL Japan) apparatus. The Brunauer–Emmett–Teller (BET) method was used to determine surface area of the catalysts. Nickel content of the catalysts was measured by ICP-AES (ICPS-100IV, Shimadzu) analyses. X-ray diffraction (XRD) experiments were performed by a D-Max2500-PC (Rigaku) instrument using Cu-Kα radiation (λ = 1.541 Å) operated at 50 kV and 100 mA. Temperature-programmed reduction (TPR) measurements were conducted using a conventional flow apparatus. For the TPR measurements, 100 mg of catalyst sample was reduced with a mixed stream of H_2 (2 ml/min) and N_2 (20 ml/min) at temperatures ranging from room temperature to 1000 °C with a ramping rate of 5 °C/min. TPR profiles were collected on a gas chromatograph (ACME 6000, Younglin) equipped with a thermal conductivity detector (TCD). Transmission electron microscopy (TEM) analyses were performed to investigate pore structure and nickel dispersion of the catalysts using a TEM instrument (JEM-2000EXII, Jeol). Hydrogen adsorption capacity and adsorption strength of the reduced catalysts were measured by H_2-TPD (temperature-programmed desorption) experiments using a BELCAT-B instrument (BEL Japan). Prior to the H_2-TPD measurements, 50 mg of catalyst sample was reduced with a mixed stream of hydrogen (2.5 ml/min) and argon (47.5 ml/min) at 650 °C for 3 h. After purging and cooling the sample to 50 °C under argon flow (50 ml/min), diluted hydrogen (5% hydrogen and 95% argon) was injected into the reduced catalyst at 50 °C for 30 min. Physisorbed hydrogen was removed under argon flow (50 ml/min) at 100 °C for 1 h. Furnace temperature was then increased from 50 °C to 1000 °C at a heating rate of 5 °C/min under a flow of argon (30 ml/min). The desorbed hydrogen was detected using a thermal conductivity detector (TCD). Adsorption stoichiometry of H/Ni = 1 and atomic cross-sectional area of 6.49×10^{-20} m^2/Ni-atom were assumed to calculate nickel surface area. Ethanol adsorption capacity of the catalysts was measured by performing EtOH-TPD experiments. Prior to the EtOH-TPD experiments, 0.1 g of catalyst sample was reduced at 650 °C for 3 h under a mixed flow of hydrogen (3 ml/min) helium (30 ml/min). After purging and cooling the sample to room temperature under helium flow (30 ml/min), 10 ml of ethanol vapor (49.7% ethanol and 50.3% helium) was pulsed into the reactor every minute under a flow of helium (5 ml/min) until the active sites were saturated with ethanol. Physisorbed ethanol was removed by evacuating the sample at 50 °C for 1 h under a flow of helium (15 ml/min). Furnace temperature was then increased from room temperature to 900 °C at a heating rate of 10 °C/min under a flow of helium (10 ml/min). The desorbed ethanol and carbon-containing products were detected using a GC-MSD (6890N GC-5975MSD, Agilent). In order to investigate carbon deposition on the used catalysts, TPO (temperature-programmed oxidation) measurements were conducted. 0.05 g of spent catalyst obtained after 1000-min reaction was used for TPO experiments. TPO measurements were performed using a GC-MSD (6890N GC-5975MSD, Agilent) with a mixed stream of O_2 (2 ml/min) and He (20 ml/min) at temperatures ranging from room temperature to 900 °C with a ramping rate of 5 °C/min.

2.3. Hydrogen production by steam reforming of ethanol

A continuous flow fixed-bed reactor system under atmospheric pressure was used to evaluate catalytic performance in the steam reforming of ethanol over SNA and SINA catalysts. Prior to the reaction, each catalyst was reduced with a mixed stream of hydrogen (3 ml/min) and nitrogen (30 ml/min) at 650 °C for 3 h. After purging the reactor with nitrogen flow (30 ml/min) for 30 min, steam reforming of ethanol was conducted at 450 °C for 1000 min. A liquid mixture of ethanol and water (1:6 molar ratio) was constantly fed to the inlet line by a syringe pump (US/KDS-101, KdScientific) at a flow rate of 1 ml/h. In order to vaporize the reactant, inlet line of the reactor was heated at 200 °C. Feed composition was fixed at C_2H_5OH:H_2O:N_2 = 1:6:12.2, and total feed rate with respect to catalyst weight was maintained at 25,910 ml/h g. The composition of outlet gases was analyzed using an on-line gas chromatograph (ACME 6000, Younglin) equipped with a thermal conductivity detector (TCD). Porapak N and Molecular Sieve 5A columns were used for product separation. Ethanol conversion, hydrogen yield, and selectivity for carbon-containing product were calculated

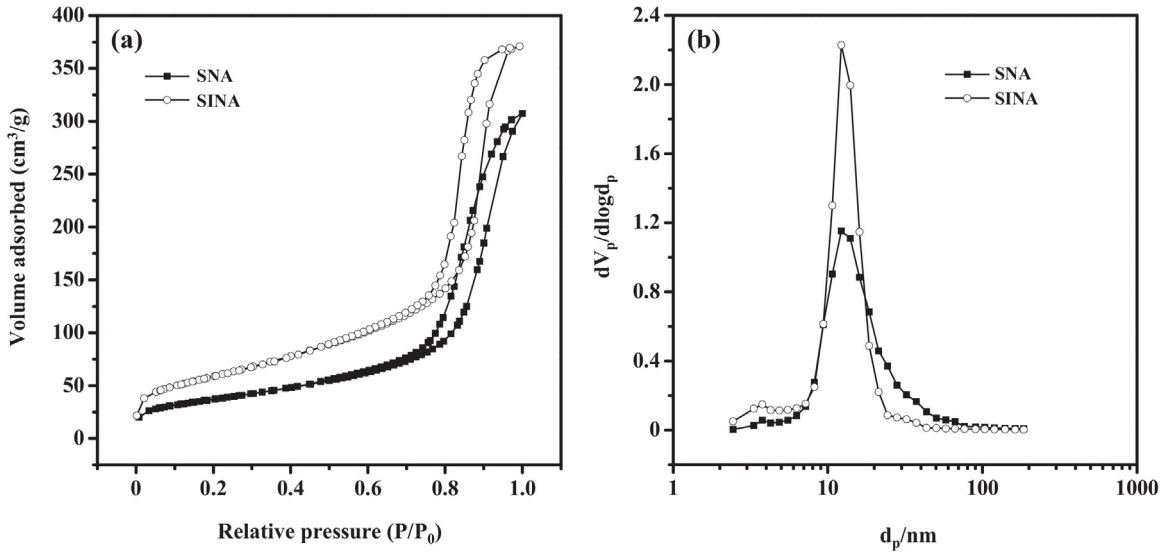

Fig. 1. (a) Nitrogen adsorption–desorption isotherms and (b) pore-size distributions of SNA and SINA catalysts calcined at 550 °C for 5 h.

according to the following equations, as defined in our previous work [29].

$$\text{Ethanol conversion}\,(\%) = \left(\frac{F_{\text{EtOH,in}} - F_{\text{EtOH,out}}}{F_{\text{EtOH,in}}}\right) \times 100 \quad (1)$$

$$\text{Hydrogen yield}\,(\%) = \frac{F_{\text{H}_2\text{,out}}}{3 \times (F_{\text{EtOH,in}} - F_{\text{EtOH,out}})} \times 100 \quad (2)$$

$$S_{i,\text{Carbon-containing product}}\,(\%) = \frac{n_i \times F_{i,\text{ Carbon-containing product}}}{2 \times (F_{\text{EtOH,in}} - F_{\text{EtOH,out}})} \times 100 \quad (3)$$

Table 1
Detailed physicochemical properties of SNA and SINA catalysts calcined at 550 °C for 5 h.

Catalyst	Ni content (wt%)[a]	Surface area (m^2/g)[b]	Pore volume (cm^3/g)[c]	Average pore diameter (nm)[d]
SNA	13.9	168	0.49	11.6
SINA	13.5	212	0.57	10.8

[a] Determined by ICP-AES measurement.
[b] Calculated by the BET equation.
[c] Total pore volume at $P/P_0 \sim 0.995$.
[d] Mean pore diameter.

3. Results and discussion

3.1. Physicochemical properties of catalysts

Textural properties of the catalysts were examined by nitrogen adsorption–desorption measurements. Nitrogen adsorption–desorption isotherms of SNA and SINA catalysts are shown in Fig. 1(a). Both catalysts exhibited type-IV isotherm and H1-type hysteresis loop. This indicates that both catalysts retained a mesoporous structure with uniform pores [30]. Fig. 1(b) shows the BJH (Barrett–Joyner–Halenda) pore size distributions of SNA and SINA catalysts obtained from desorption branches. SNA catalyst showed a monomodal distribution centered at around 10 nm. On the other hand, SINA catalyst exhibited a major distribution centered at around 10 nm and a minor distribution centered at around 3 nm. It is inferred that mesopores at around 10 nm was due to compound micelles of block copolymer with ionic liquid

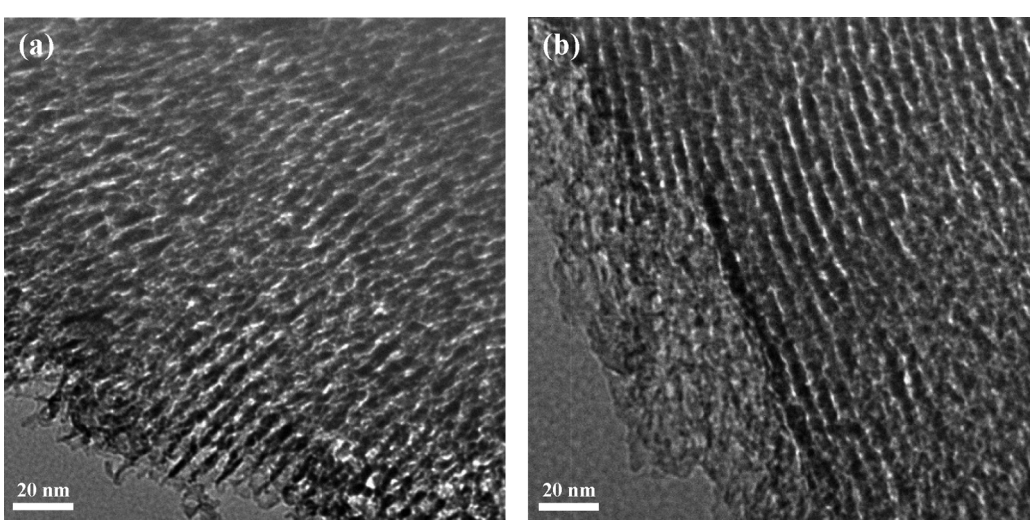

Fig. 2. TEM images of (a) SNA and (b) SINA catalysts calcined at 550 °C for 5 h.

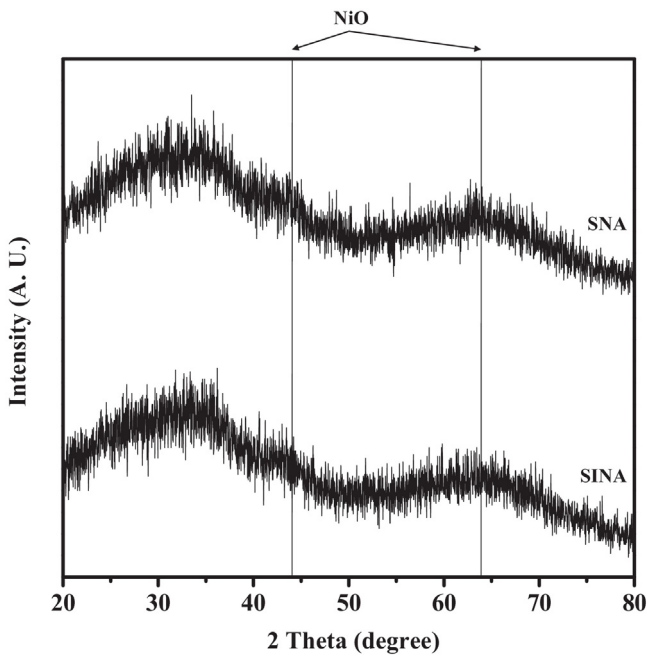

Fig. 3. XRD patterns of SNA and SINA catalysts calcined at 550 °C for 5 h.

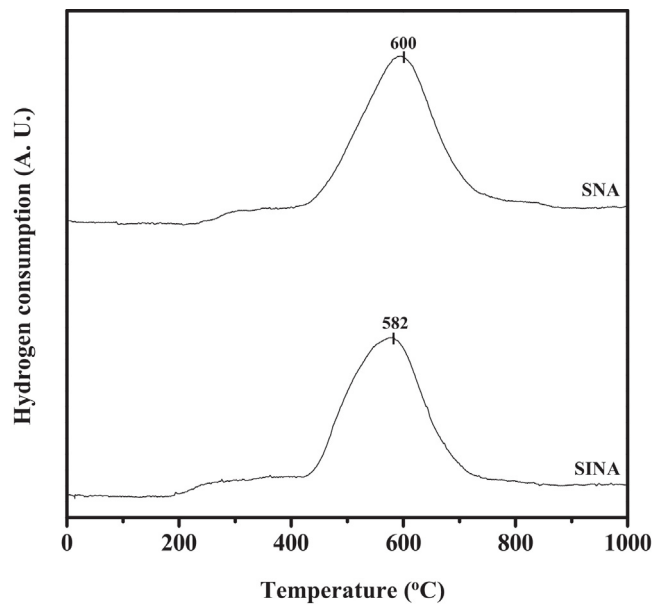

Fig. 4. TPR profiles of SNA and SINA catalysts calcined at 550 °C for 5 h.

while mesopores at around 3 nm was due to individual micelles of ionic liquid.

Detailed textural properties of the catalysts determined from the isotherms are presented in Table 1. ICP-AES results showed that nickel content of the catalysts was quite similar to the designed value. It was also observed that SINA catalyst retained higher surface area, larger pore volume, and smaller average pore diameter than SNA catalyst. Considering the pore size distribution, it is inferred that large pore volume of SINA catalyst was mainly attributed to the increase of mesopores at around 10 nm. On the other hand, high surface area of SINA catalyst was due to the increase of mesopores at around 3 nm, which interconnected large mesopores [21,31].

In order to investigate pore structure of the catalysts, TEM analyses were conducted. Fig. 2 shows the TEM images of SNA (Fig. 2(a)) and SINA (Fig. 2(b)) catalysts calcined at 550 °C. It was observed that both catalysts retained a rod-like mesoporous structure. The rod-like mesopores were formed by the removal of cylindrical micelle assembly through thermal decomposition of micelle during the evaporation-induced self-assembly process. Thus, the rod-like mesoporous structure was successfully formed in both catalysts via evaporation-induced self-assembly method as attempted in this work [16].

3.2. XRD and TPR results

XRD patterns of SNA and SINA catalysts calcined at 550 °C for 5 h are presented in Fig. 3. Both catalysts exhibited weak crystalline phase of NiO (solid lines in Fig. 3) but they showed no distinct crystalline phase of Al_2O_3, indicating that highly dispersed NiO was formed in amorphous Al_2O_3 structure in both catalysts. This can be explained by the fact that co-existence of Al_2O_3 and NiO can retard crystallization during the calcination process [32].

TPR measurements were conducted to investigate the metal-support interaction in the SNA and SINA catalysts as presented in Fig. 4. Both catalysts retained a single reduction band at around 590 °C with no great difference. Considering the XRD results of calcined catalysts (Fig. 3), it can be inferred that the reduction band of SNA and SINA catalysts was related to the reduction of NiO interacted with Al_2O_3 support.

Fig. 5 shows the XRD patterns of SNA and SINA catalysts reduced at 650 °C. Both catalysts exhibited diffraction peaks corresponding to metallic Ni (solid lines in Fig. 5) but they showed no diffraction peaks corresponding to NiO. This means that NiO species in the SNA and SINA catalysts were completely reduced into metallic nickel during the reduction process employed in this work. Nickel particle size of reduced catalysts was calculated from Ni (1 1 1) peak in Fig. 5 using the Scherrer equation as listed in Table 2. It was found that nickel particle size of SINA catalyst was slightly smaller than that of SNA catalyst.

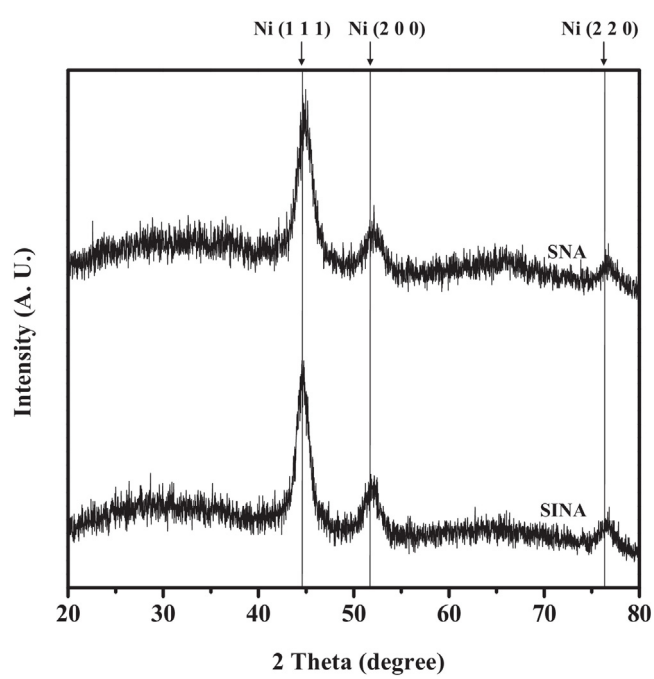

Fig. 5. XRD patterns of SNA and SINA catalysts reduced at 650 °C for 3 h.

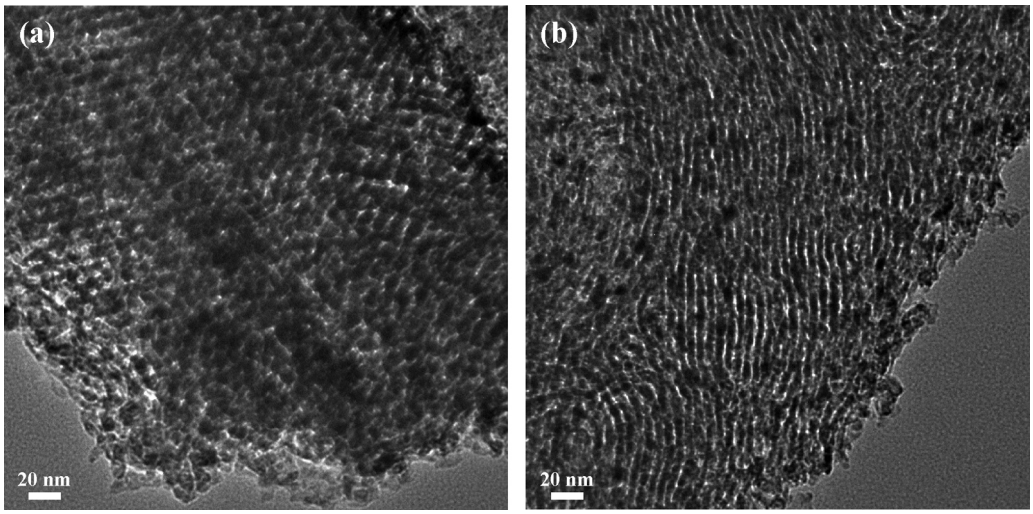

Fig. 6. TEM images of (a) SNA and (b) SINA catalysts reduced at 650 °C for 3 h.

Table 2
Nickel particle size of reduced SNA and SINA catalysts.

Catalyst	Nickel particle size (nm)[a]
SNA	5.5
SINA	5.3

[a] Calculated from Ni (1 1 1) diffraction peak in Fig. 5.

3.3. Ni dispersion in the reduced catalysts

Fig. 6 shows the TEM images of SNA (Fig. 6(a)) and SINA (Fig. 6(b)) catalysts reduced at 650 °C. It was observed that metallic nickel was well dispersed in the SINA catalyst, while aggregation of metallic nickel was observed in the SNA catalyst. In addition, rod-like mesopores in the SINA catalyst were better conserved than those in the SNA catalyst. Accordingly, it can be inferred that the addition of ionic liquid in the preparation of SINA catalyst not only increased thermal resistance of pore structure but also improved nickel dispersion of SINA catalyst.

H_2-TPD experiments were performed over SNA and SINA catalysts in order to determine the nickel surface area of the catalysts. According to the previous reports [33,34], hydrogen not only forms a monolayer on the active metal but also migrates to the subsurface layer or undergoes spillover. For quantitative analysis, therefore, H_2-TPD profiles of the catalysts were deconvoluted into three domains as presented in Fig. 7. The amounts of H_2 desorbed from weak site (<300 °C) and strong site (300–600 °C) were calculated from each deconvoluted area in the H_2-TPD profiles as summarized in Table 3. Here, the desorbed peak appearing above 600 °C, which was attributed to hydrogen migration to subsurface layer or spillover, was excluded in the calculation of nickel surface area. Nickel surface area was then calculated from total weak and strong peak areas of H_2-TPD profiles. It was observed that SINA catalyst retained larger amount of hydrogen desorption and higher nickel surface area than SNA catalyst. In particular, SINA catalyst with higher nickel surface area retained larger amount of strong hydrogen-binding sites. This is because the addition of ionic liquid increased dispersion of nickel species by acting as a spacer, which increased adsorption sites for intimate contact with nickel crystallites [35]. Thus, it can be inferred that higher dispersion of nickel particles in the SINA catalyst was responsible for its higher nickel surface area, in good agreement with XRD and TEM results.

Table 3
H_2-TPD results for reduced SNA and SINA catalysts.

Catalyst		SNA	SINA
Amount of H_2 desorbed (μmol-H_2/g)[a]	Weak site (<300 °C)	26.2 (43.6%)[b]	32.8 (41.5%)[b]
	Strong site (300–600 °C)	33.9 (56.4%)[b]	46.2 (58.5%)[b]
	Total	60.1	79.0
Nickel surface area (m^2/g-Ni)[c]		31.3	41.1

[a] Calculated from peak area of H_2-TPD profiles in Fig. 7.
[b] Values in parentheses are percentage of each deconvoluted area in the H_2-TPD profiles.
[c] Calculated by assuming $H/Ni_{atom} = 1$.

3.4. Ethanol adsorption study on the reduced catalysts

In order to investigate the ethanol adsorption capacity and reaction mechanism, EtOH-TPD measurements were conducted. Fig. 8 shows the EtOH-TPD profiles of SNA (Fig. 8(a)) and SINA (Fig. 8(b)) catalysts. Both catalysts showed profiles for ethanol ($m/z = 31$), methane ($m/z = 16$), acetaldehyde ($m/z = 29$), carbon monoxide ($m/z = 28$), and carbon dioxide ($m/z = 44$). Both catalysts exhibited peaks for molecularly desorbed ethanol and acetalde-

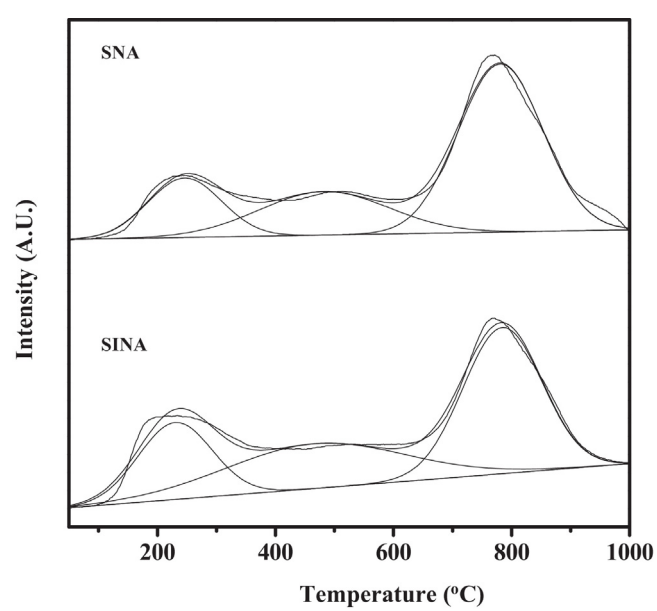

Fig. 7. H_2-TPD profiles of SNA and SINA catalysts reduced at 650 °C for 3 h.

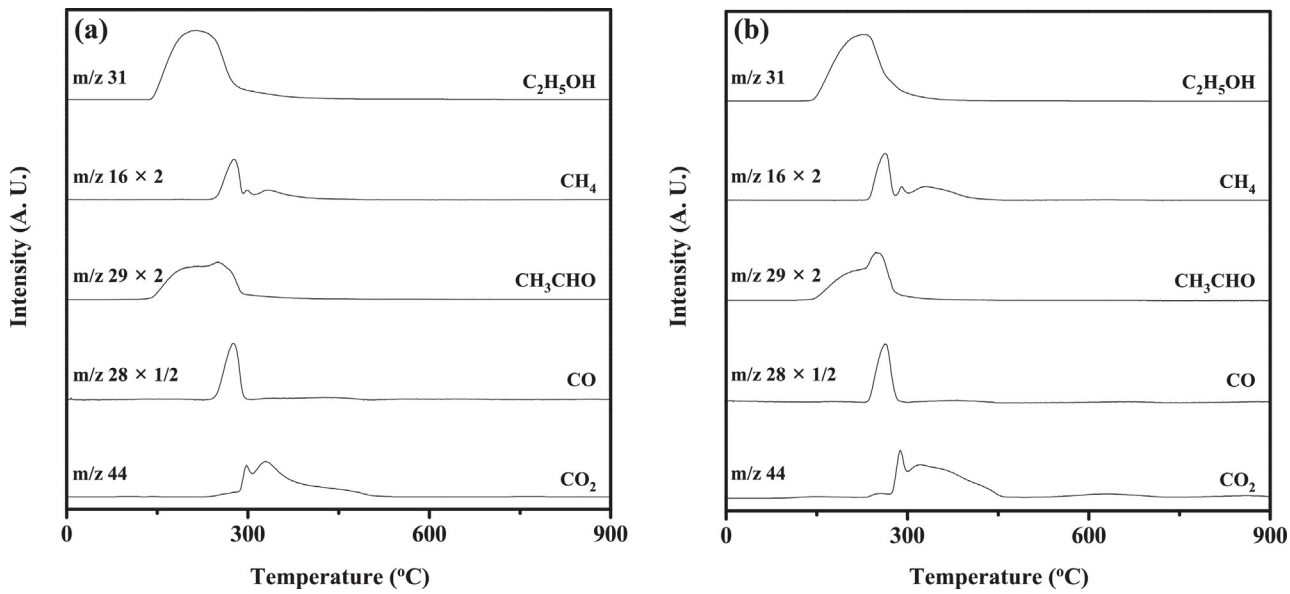

Fig. 8. EtOH-TPD profiles of (a) SNA and (b) SINA catalyst reduced at 650 °C for 3 h.

hyde at temperature range of 150–300 °C. This indicates that dehydrogenation of ethanol ($C_2H_5OH \leftrightarrow CH_3CHO + H_2$) via selective C—H bond cleavage of surface ethoxides occurred at low temperature [36,37]. On the other hand, peaks for methane and carbon monoxide appeared at around 280 °C, indicative of decomposition of acetaldehyde ($CH_3CHO \leftrightarrow CO + CH_4$) [36,37]. Peaks for methane were also observed above 300 °C, which was caused by decomposition of acetaldehyde ($CH_3CHO \leftrightarrow CO + CH_4$). Concurrently, peaks for carbon dioxide were detected instead of carbon monoxide, demonstrating that Boudouard reaction ($2CO \leftrightarrow CO_2 + C$) occurred dominantly at temperatures above 300 °C [38,39]. Therefore, it can be deduced that bond breakage of ethanol on nickel active sites occurred in the following order; O—H bond scission in adsorbed ethanol, C—H bond scission in adsorbed ethoxides, and C—C bond scission in adsorbed acetaldehyde [40,41].

To determine total amount of adsorbed ethanol, the amount of each molecule was quantified from EtOH-TPD profiles in Fig. 8, as summarized in Table 4. It was observed that both catalysts retained large amount of molecularly desorbed ethanol, which was attributed to large ethanol adsorption capacity of Al_2O_3. Although SINA catalyst showed larger total amount of ethanol adsorption than SNA catalyst, the amounts of ethanol and acetaldehyde desorbed from SINA catalyst were smaller than those from SNA catalyst. This indicates that SINA catalyst retained large amount of active sites which led to decomposition and dehydration, resulting in low residence time of reaction intermediates. It has been reported that ethanol is adsorbed not only on the Lewis acid sites of alumina support but also on the active phase of the catalyst [42]. Because BET surface area is related to the adsorption sites of alumina support and nickel surface area is related to the adsorption sites of active phase, both BET surface area and nickel surface area are related to the ethanol adsorption capacity.

Table 4
EtOH-TPD results for reduced SNA and SINA catalysts.

Catalyst		SNA	SINA
Amount of desorption (mmol/g)[a]	EtOH	0.47	0.40
	CH_4	0.28	0.43
	CH_3CHO	0.075	0.069
	CO	0.23	0.23
	CO_2	0.38	0.50
Total amount of ethanol adsorbed (mmol/g)[a]		0.99	1.05

[a] Calculated from peak area of EtOH-TPD profiles in Fig. 8.

3.5. Hydrogen production by steam reforming of ethanol

Fig. 9 shows the hydrogen yields with time on stream over SNA and SINA catalysts in the steam reforming of ethanol at 450 °C. Both catalysts exhibited a stable performance without severe deactivation due to their well-developed mesoporous structure. Although both catalysts showed a stable performance with time on stream, SINA catalyst exhibited higher hydrogen yield than SNA catalyst in the steam reforming of ethanol.

Detailed catalytic performance of SNA and SINA catalysts in the steam reforming of ethanol at 450 °C obtained after a 1000-min reaction is summarized in Table 5. It was revealed

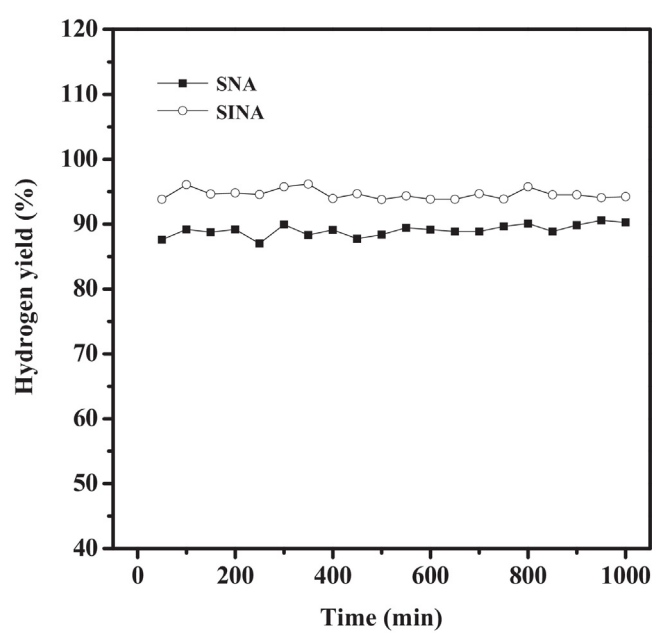

Fig. 9. Hydrogen yields with time on stream in the steam reforming of ethanol over SNA and SINA catalysts at 450 °C. All the catalysts were reduced at 650 °C for 3 h prior to the reaction.

Table 5
Detailed catalytic performance of SNA and SINA catalysts in the steam reforming of ethanol at 450 °C after a 1000 min-reaction.

Catalyst	Ethanol conversion (%)	Hydrogen yield (%)	Selectivity (%)		
			CH_4	CO	CO_2
SNA	100	90.3	35.6	10.5	53.9
SINA	100	94.2	35.4	8.1	56.5

that both catalysts showed complete conversion of ethanol. Carbon-containing compounds such as methane, carbon monoxide, and carbon dioxide were produced as by-products. Carbon-containing compounds were formed by additional reactions during the steam reforming of ethanol such as ethanol decomposition ($C_2H_5OH \rightarrow CH_4 + CO + H_2$) and steam reforming of ethanol to syngas ($C_2H_5OH + H_2O \rightarrow 2CO + 4H_2$) [43]. Interestingly, ethylene was not observed over both SNA and SINA catalysts. Ethylene is an intermediate product formed by dehydration of ethanol ($C_2H_5OH \rightarrow C_2H_4 + H_2O$), which serves as a main precursor of coking. Therefore, it can be inferred that both catalysts retained high stability in the steam reforming of ethanol because dehydration of ethanol was suppressed during the reaction over the catalysts. On the other hand, SINA catalyst retained higher selectivity for carbon dioxide than SNA catalyst. This indicates that higher hydrogen yield over SINA catalyst was also attributed to higher reactivity of water–gas shift reaction ($CO + H_2O \rightarrow H_2 + CO_2$).

Fig. 10 shows the temperature-programmed oxidation (TPO) results of spent SNA and SINA catalysts. Major oxidation peak of SNA catalyst appeared at 627 °C while that of SINA catalyst appeared at 598 °C. This indicates that carbon filaments formed on the SINA catalyst were oxidized more easily than those formed on the SNA catalyst. It is known that coke gasification is much favorable on the catalyst with high surface area and large pore volume because of pore diffusion limitation in the coke gasification reaction [44]. It was also observed that the area of TPO peak of SNA catalyst was larger than that of SINA catalyst. This can be explained by the fact that SNA catalyst with low nickel surface area retained high residence time of coke precursors, which increased the probability of coke polymerization [45,46].

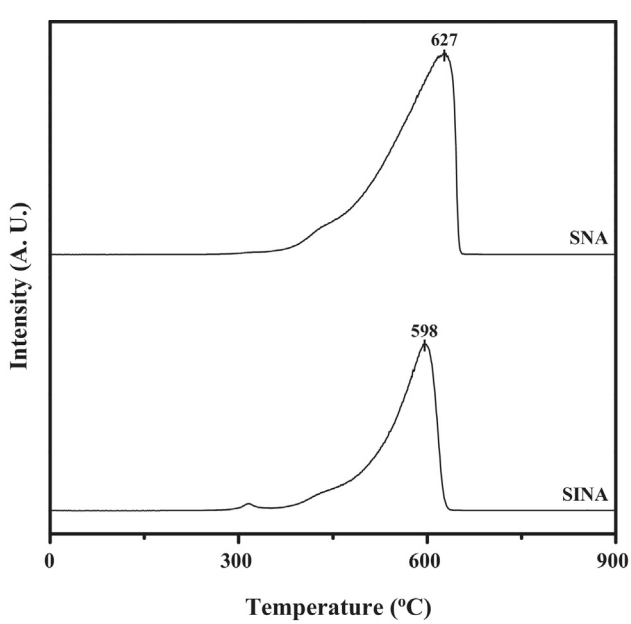

Fig. 10. TPO profiles of spent SNA and SINA catalysts.

4. Conclusions

A dual-templated Ni–Al_2O_3 catalyst (SINA) was prepared by a single-step evaporation-induced self-assembly (EISA) method using P123 and ionic liquid as templates. For comparison, a P123-templated Ni–Al_2O_3 (SNA) was also prepared by a single-step evaporation-induced self-assembly (EISA) method. The effect of ionic liquid addition on the physicochemical properties and catalytic activities of the catalysts was investigated. It was revealed that both catalysts retained a well-developed mesoporous structure. H_2-TPD experiments revealed that SINA catalyst retained higher nickel surface area than SNA catalyst. In addition, SINA catalyst retained higher ethanol adsorption capacity than SNA catalyst. In the hydrogen production by steam reforming ethanol, both catalysts exhibited a stable catalytic performance without severe deactivation. However, SINA catalyst showed higher hydrogen yield than SNA catalyst. The superior catalytic performance of SINA catalyst was due to its high surface area and high nickel dispersion. Therefore, it was concluded that the addition of ionic liquid as a co-template increased surface area, nickel dispersion, and catalytic activity of SINA catalyst.

Acknowledgements

This work was supported by the Global Frontier R&D Program on Center for Multiscale Energy System funded by the National Research Foundation under the Ministry of Science, ICT & Future Planning, Korea (20110031575).

References

[1] M.S. Dresselhaus, I.L. Thomas, Nature 414 (2001) 332–337.
[2] R.D. Cortright, R.R. Davda, J.A. Dumesic, Nature 418 (2002) 964–967.
[3] A. Midilli, M. Ay, I. Dincer, M.A. Rosen, Renew. Sustain. Energy Rev. 9 (2005) 255–271.
[4] A.N. Fatsikostas, D.I. Kondarides, X.E. Verykios, Chem. Commun. (2001) 851–852.
[5] V. Klouz, V. Fierro, P. Denton, H. Katz, J.P. Lisse, S. Bouvot-Mauduit, C. Mirodatos, J. Power Sources 105 (2002) 26–34.
[6] J.L. Contreras, J. Salmones, J.A. Colín-Luna, L. Nuño, B. Quintana, I. Córdova, B. Zeifert, C. Tapia, G.A. Fuentes, Int. J. Hydrogen Energy 39 (2014) 18835–18853.
[7] M.C. Sánchez-Sánchez, R.M. Navarro, J.L.G. Fierro, Int. J. Hydrogen Energy 32 (2007) 1462–1471.
[8] A.L. Alberton, M.M.V.M. Souza, M. Schmal, Catal. Today 123 (2007) 257–264.
[9] G. Rabenstein, V. Hacker, J. Power Sources 185 (2008) 1293–1304.
[10] M.E.S. Hegarty, A.M. O'Connor, J.R.H. Ross, Catal. Today 42 (1998) 225–232.
[11] S. Therdthianwong, A. Therdthianwong, C. Siangchin, S. Yongprapat, Int. J. Hydrogen Energy 33 (2008) 991–999.
[12] J.G. Seo, M.H. Youn, K.M. Cho, S. Park, S.H. Lee, J. Lee, I.K. Song, Korean J. Chem. Eng. 25 (2008) 41–45.
[13] M.E. Davis, Nature 417 (2002) 813–821.
[14] S.C. Warren, L.C. Messina, L.S. Slaughter, M. Kamperman, Q. Zhou, S.M. Gruner, F.J. DiSalvo, U. Wiesner, Science 320 (2008) 1748–1752.
[15] Y. Deng, J. Wei, Z. Sun, D. Zhao, Chem. Soc. Rev. 42 (2013) 4054–4070.
[16] Y. Bang, S.J. Han, J.G. Seo, M.H. Youn, J.H. Song, I.K. Song, Int. J. Hydrogen Energy 37 (2012) 17967–17977.
[17] J.Y. Ying, C.P. Mehnert, M.S. Wong, Angew. Chem. Int. Ed. 38 (1999) 56–77.
[18] U. Ciesla, F. Schüth, Microporous Mesoporous Mater. 27 (1999) 131–149.
[19] T. Brezensinski, C. Erpen, K. Iimura, B. Smarsly, Chem. Mater. 17 (2005) 1683–1690.
[20] C. Liu, S. Wang, Z. Rong, X. Wang, G. Gu, W. Sun, J. Non-Cryst. Solids 356 (2010) 1246–1251.
[21] O. Sel, D. Kuang, M. Thommes, B. Smarsly, Langmuir 22 (2006) 2311–2322.
[22] Y. Zhou, M. Antonietti, Chem. Commun. (2003) 2564–2565.
[23] Y. Zhou, J.H. Schattka, M. Antonietti, Nano Lett. 4 (2004) 477–481.
[24] J. Yuan, X. Bai, M. Zhao, L. Zheng, Langmuir 26 (2010) 11726–11731.
[25] Z. Ma, J. Yu, S. Dai, Adv. Mater. 22 (2010) 261–285.
[26] T. Wang, H. Kaper, M. Antonietti, B. Smarsly, Langmuir 23 (2007) 1489–1495.
[27] Y. Zhou, M. Antonietti, Adv. Mater. 15 (2003) 1452–1455.
[28] K. Zhu, F. Požgan, L. D'Souza, R.M. Richards, Microporous Mesoporous Mater. 91 (2006) 40–46.
[29] S.J. Han, Y. Bang, J.G. Seo, J. Yoo, I.K. Song, Int. J. Hydrogen Energy 38 (2013) 1376–1383.

[30] G. Leofanti, M. Padovan, G. Tozzola, B. Venturelli, Catal. Today 41 (1998) 207–219.
[31] D. Kuang, T. Brezesinski, B. Smarsly, J. Am. Chem. Soc. 126 (2004) 10534–10535.
[32] W.O. Milligan, L. Merten, J. Phys. Chem. 50 (1946) 465–470.
[33] S. Velu, S.K. Gangwal, Solid State Ionics 177 (2006) 803–811.
[34] S.J. Han, Y. Bang, J. Yoo, S. Park, K.H. Kang, J.H. Choi, J.H. Song, I.K. Song, Int. J. Hydrogen Energy 39 (2014) 10445–10453.
[35] C.H. Bartholomew, Catal. Lett. 7 (1990) 27–52.
[36] P.-Y. Sheng, G.A. Bowmaker, H. Idriss, Appl. Catal. A 261 (2004) 171–181.
[37] A.N. Fatsikostas, X.E. Verykios, J. Catal. 225 (2004) 439–452.
[38] P.D. Vaidya, A.E. Rodrigues, Chem. Eng. 117 (2006) 39–49.
[39] A. Haryanto, S. Fernando, N. Murali, S. Adhikari, Energy Fuels 19 (2005) 2098–2106.
[40] Y.-J. Wu, J.C. Santos, P. Li, J.-G. Yu, A.F. Cunha, A.E. Rodrigues, Can. J. Chem. Eng. 92 (2014) 116–130.
[41] H. Song, X. Bao, C.M. Hadad, U.S. Ozkan, Catal. Lett. 141 (2011) 43–54.
[42] S. Cai, K. Sohlberg, J. Mol. Catal. A: Chem. 193 (2003) 157–164.
[43] M. Benito, J.L. Sanz, R. Isabel, R. Padilla, R. Arjona, L. Daza, J. Power Sources 151 (2005) 11–17.
[44] D.L. Trimm, Catal. Rev. Sci. Eng. 16 (1977) 155–189.
[45] P. Forzatti, L. Lietti, Catal. Today 52 (1999) 165–181.
[46] C.H. Bartholomew, Appl. Catal. A 212 (2001) 17–60.